International Journal of Nanomedicine

Dovepress
open access to scientific and medical research

Open Access Full Text Article

ORIGINAL RESEARCH

"Shell-Core" Bilayer Nanoparticle as Chemotherapeutic Drug Co-Delivery Platforms Render Synchronized Microenvironment Respond and Enhanced Antitumor Effects

Jia Zeng[1], Peng Sun[1], Xinning Fang[1], Yicheng Jiang[1], Zhenghong Wu[1], Xiaole Qi[1,2]

[1]Key Laboratory of Modern Chinese Medicines, China Pharmaceutical University, Nanjing, People's Republic of China; [2]Industrial Technology Innovation Platform, Zhejiang Center for Safety Study of Drug Substances, Hangzhou, People's Republic of China

Correspondence: Zhenghong Wu; Xiaole Qi, Key Laboratory of Modern Chinese Medicines, China Pharmaceutical University, No. 639 Longmian Road, Jiangning District, Nanjing City, Jiangsu Province, 210009, People's Republic of China, Tel +86 15062208341; +86 25 83179703, Email zhenghongwu66@cpu.edu.cn; qixiaole523@cpu.edu.cn

Background: Synergistic chemotherapy has been proved as an effective antitumor means in clinical practice. However, most co-administration treatment often lacks simultaneous control over the release of different chemotherapeutic agents.

Materials and Methods: β-cyclodextrin modified hyaluronic acid was the "shell", and the oxidized ferrocene-stearyl alcohol micelles served as the "core", where doxorubicin (DOX) and curcumin (CUR) were loaded in shell and core of the bilayer nanoparticles (BNs), respectively. The pH- and glutathione (GSH)-responsive synchronized release behavior was evaluated in different mediums, and the in vitro and in vivo synergistic antitumor effect and CD44-mediated tumor targeting efficiency were further investigated.

Results: These BNs had a spherical structure with the particle size of 299 ± 15.17 nm, while the synchronized release behaviour of those two drugs was proved in the medium with the pH value of 5.5 and 20 mM GSH. The co-delivery of DOX and CUR reduced the IC_{50} value by 21% compared to DOX alone, with a further 54% reduction after these BNs delivery measurements. In tumor-bearing mouse models, these drug-loaded BNs showed significant tumor targeting, enhanced antitumor activity and reduced systemic toxicity.

Conclusion: The designed bilayer nanoparticle could be considered as potential chemotherapeutic co-delivery platform for efficient synchronized microenvironment respond and drug release. Furthermore, the simultaneous and synergistic drug release guaranteed the enhanced antitumor effects during the co-administration treatment.

Keywords: tumor microenvironment, combination chemotherapy, pH- and GSH-responsive, tumor targeting

Introduction

Tumor microenvironment (TME) is closely related to the occurrence, development and metastasis of tumors, and has been attracting great research interest as a target for tumor therapy.[1–3] TME comprises diverse non-cancerous cells and immune cells, which can support cancer cells to sustain the infinite proliferation and escape from the natural apoptotic pathways, as well as TME contains non-cellular components including extracellular matrix (ECM), various cytokines and chemokines, which guarantee the process of angiogenesis and invasion.[4–6] TME exhibits unique reduction and acidic conditions due to the cells' own metabolic activities and nutritional demands.[7–9] Compared with normal tissues, a lower pH exists in tumor tissues, while the concentrations of glutathione (GSH) are significantly higher. Nevertheless, the compositions of TME collectively or cooperatively hinder the drug distribution, leading to abnormal tumor cell proliferation and anticancer drug resistance.[10] Therefore, targeting and modulating TME is a potential strategy for antitumor therapy, such as targeting cancer-associated fibroblasts and tumor infiltrating immune cells, or responding to the specific microenvironmental conditions.[11–13] These targeting or responsive behaviors facilitate augmented release and efficient distribution, finally enhancing the drug accumulation in tumor sites.[14]

Received: 25 December 2022
Accepted: 27 February 2023
Published: 24 March 2023

Graphical Abstract

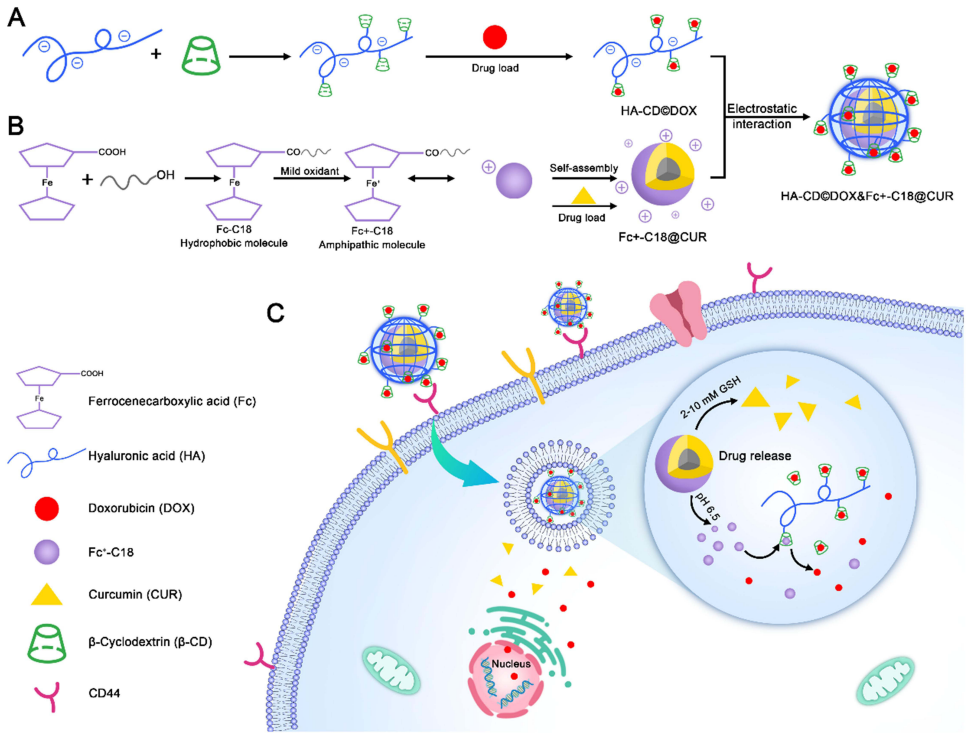

Multiple stimulus responsive drug delivery nanoparticles, in particular, offer a superior approach to improving anticancer therapeutic effects due to their high sensitivity to multiple cancerous stimuli, such as pH, light, reduction and enzymes.[15–17] Moreover, nanoparticles with long systemic circulation tend to accumulate in tumor tissues, while the surface charge greatly affects the distribution and retention behavior of nanoparticles in vivo.[18–20] Negatively charged drug carrier particles are less prone to be cleared by mononuclear phagocyte system, since the cell membrane is negatively charged.[21,22]

In addition, the combination of drugs with different mechanisms can synergistically enhance the antitumor therapeutic effects. On the one hand, multidrug resistance (MDR) increases the efflux of multiple chemotherapeutic agents, leading to the decrease in intracellular drug levels, thereby limiting efficacy.[23,24] Therefore, the synergistic delivery of chemotherapeutic agents and MDR inhibitors is expected to be an effective strategy in overcoming MDR.[25] Remarkably, overexpression of glutathione S-transferase (GST) in tumor cells also confer high levels of resistance, so the GSH depletion can alleviate resistance to some extent and reduce the dose administrated.[26,27] On the other hand, for non-targeting drugs, combination chemotherapy reduces the toxicity and exerts chemoprotections.[28] Consequently, the design of co-delivery vectors that efficiently respond to TME is essential for antitumor therapy.

Herein, we have designed a bilayer "shell-core" nanoparticle structure for the co-delivery of two drugs in combination chemotherapy. We selected Doxorubicin (DOX) and curcumin (CUR) as co-delivery drug models, in which CUR can reduce MDR protein expressions, and attenuate the nonspecific systemic toxic effects of DOX.[28–31] Hyaluronic acid (HA) modified with β-cyclodextrin (β-CD) is considered as the outer 'shell' (HA-CD), and the oxidized form of ferrocene (Fc) combined with stearyl alcohol (C_{18}) can self-assemble to form micelles as the inner "core" (Fc^{+}-C_{18}), where DOX and CUR are separately encapsulated into shell and core. Subsequently, negative charged HA-CD shell will spontaneously bind to Fc^{+}-C_{18} core, forming 'shell-core' bilayer nanoparticles (BNs) (HA-CD@DOX & Fc-C_{18}@CUR).

HA-coated BNs exhibit electronegativity as a whole, enhancing the long systemic circulation in vivo, and HA can also achieve active targeting to $CD44^{+}$ tumor cells.[32] Passive enhanced permeability and retention effect (EPR) and

active CD44-mediated targeting allow BNs accumulate at the tumor sites, where BNs rapidly respond to the high concentration of H^+ and GSH. The linkage between HA and *β*-CD is pH-sensitive, while the Fc group is prone to hydrophilic-hydrophobic reversal under redox conditions. Free Fc groups further compete for the hydrophobic cavity of *β*-CD, accelerating DOX release. Summarily, we propose a tumor-targeted and TME-responsive combination drug delivery platform with enhanced long circulation ability.

Materials and Methods

Materials

Sodium hyaluronate (MW = 3.4 KDa) was obtained from Freda Biopharm (Jinan, China). *β*-Cyclodextrin (*β*-CD) was purchased from Titan Technology Co., Ltd. (Shanghai, China). Ion exchange resin (Dowex 50W×8-400) was gained from Dow Chemical Company (USA). Doxorubicin hydrochloride (DOX·HCl) was bought from Sigma-Aldrich (USA). Curcumin (CUR) was gained from Yuanye Biotechnology Co., Ltd. (Shanghai, China). Ferrocene carboxylic acid (Fc), 1-(3-Dimethylaminopropyl)-3-ethylcarbodiimide hydrochloride (EDC), Tetrabutylammonium hydroxide solution (TBA), P-toluenesulfonyl chloride (PTSC), 1,6-Hexanediamine (HDA) and Carter Condensing Agent (BOP) were obtained from Aladdin Biochemical Technology Co., Ltd. (Shanghai, China). Stearyl Alcohol (C_{18}) were purchased from Lingfeng Chemical Reagent Co., Ltd. (Shanghai, China). Other chemicals and reagents used in the study were of analytical grade.

Synthesis and Characterization of HA-CD

The synthesis process was carried out in three steps which has been improved on the basis of previously reported method.[33,34] The first step was to synthesize the tetrabutylammonium salt of hyaluronic acid (HA-TBA). Washed ion exchange resin was mixed with 24.5 mL of TBA for 30 min at room temperature. After removing the supernatant, the treated resin was mixed with 1 g of HA dissolved in 100 mL water, stirring for 3 h. HA-TBA solution was obtained through filtration, and HA-TBA solid was gained by lyophilized.

Subsequently, the second step was the synthesis of amino-modified *β*-CD (NH_2-*β*-CD). 20 g *β*-CD was dispersed in 250 mL water, and NaOH solution was added dropwise and stirred for 1 h at room temperature. Keeping the reaction temperature at 0 °C, the PTSC solution dissolved in acetonitrile (5.04 g/15 mL) was continued to be slowly added and stirred for another 3 h at room temperature. Next, the filtrate was extracted and adjusted to pH 8 with HCl solution, accompanied by a large amount of white precipitate. The mixture solution stood overnight at 4 °C to obtain a white paste, which was further heated in vacuum to collect 6-o-monotosyl-6-deoxy-β-cyclodextrin (Tos-*β*-CD). Lastly, 5 g Tos-*β*-CD and 20 g HAD were mixed in 25 mL DMF and reacted in nitrogen at 80 °C for 18 h, before being poured into cold acetone for precipitation. The precipitate was washed by redissolved in methanol aqueous solution (v/v = 1:3), then dried to obtain NH_2-*β*-CD.

In the third step, HA-TBA and NH_2-*β*-CD were coupled via amination to prepare HA-CD. 1.25 g of HA-TBA and 1.5 g NH_2-β-CD were dissolved in 60 mL DMSO in nitrogen-atmosphere, and 0.53 g of BOP dissolved in 2 mL of DMSO was then added. The reaction was carried out at room temperature for 2 h. After dialysis and lyophilization, the final product was obtained.

To verify the successful synthesis of HA-CD, suitable amounts of HA, *β*-CD and HA-CD were separately dissolved in deuterium generation of water and DMSO, then tested by hydrogen-nuclear magnetic resonance (^{1}H-NMR).

DOX Loading and Characterization of HA-CD@DOX

DOX·HCl was first desalted with triethylamine before it could be incorporated into the hydrophobic cavity *β*-CD. DOX and HA-CD were mixed according to different mass ratios (1:10, 2:10, and 3:10), stirring for 24 h at room temperature, then HA-CD@DOX was obtained by dialysis and lyophilization. Subsequently, DOX, HA-CD, the physical mixture of DOX and HA-CD, and HA-CD@DOX were separately scanned by Fourier transform infrared spectroscopy (FTIR) and differential scanning calorimetry (DSC) to confirm the successful encapsulation of DOX into *β*-CD.

To evaluate the drug loading efficiency and encapsulation efficiency, the structure of HA-CD@DOX was destroyed by organic solvent, and then the concentration of dissociated DOX was tested by ultraviolet (UV) spectrophotometer. Moreover, the Zeta potential of HA-CD@DOX was measured.

Synthesis and Characterization of Fc^{+}-C_{18} Micelles

Briefly, 5.0 mg of Fc dissolved in dichloromethane mixed with 20 mg DMAP and 5 mg C_{18}, then 20 mg EDC dissolved in dichloromethane were added, stirring at room temperature for 24 h. After dialysis and lyophilization, the Fc-C_{18} was obtained. To verify the successful synthesis of Fc-C_{18}, suitable amounts of Fc, C_{18} and Fc-C_{18} were separately dissolved in deuterium generation of chloroform and DMSO, then tested by ^{1}H-NMR.

To prepare Fc-C_{18} micelles, Fc-C_{18} was oxidized by ferric chloride solution to form an amphipathic structure of Fc^{+}-C_{18} with the capability to self-assembly. After rotary evaporation, Fc^{+}-C_{18} was redissolved in water, followed with dialysis to gain the micelles, of which the formation was verified by the Tyndall effect. The particle size of Fc^{+}-C_{18} micelles was measured by dynamic light scattering (DLS), and the critical micelle concentration (CMC) was determined through pyrene fluorescent probe method.

CUR Loading and Characterization of Fc^{+}-C_{18}@CUR Micelles

CUR and Fc^{+}-C_{18} micelles were mixed according to different mass ratios (1:6, 1.5:6, 2:6), stirring for 24 h at room temperature, then Fc^{+}-C_{18}@CUR was obtained by dialysis and lyophilization. To further evaluate the drug loading efficiency and encapsulation efficiency, the structure of Fc^{+}-C_{18}@CUR was destroyed by organic solvent, and then the concentration of dissociated CUR was tested by high performance liquid chromatography (HPLC). Moreover, the particle size of Fc^{+}-C_{18}@CUR was measured.

Preparation and Characterization of HA-CD@DOX & Fc^{+}-C_{18}@CUR BNs

According to the above results, the optimal mass ratio of HA-CD@DOX and Fc^{+}-C_{18}@CUR were 2:10 and 1:6, respectively. Utilizing the electrostatic interaction, HA-CD@DOX and Fc^{+}-C_{18}@CUR solutions were evenly mixed with different concentration (1:1, 1:2, and 1:3) to prepare HA-CD@DOX & Fc^{+}-C_{18}@CUR BNs. The morphology of HA-CD@DOX & Fc^{+}-C_{18}@CUR BNs was evaluated by transmission electron microscopy (TEM), while the particle size and Zeta potential was measured. To further test the stability, HA-CD@DOX & Fc+-C_{18}@CUR solution was placed in a cilin bottle, storing in 4°C, then the particle size at different time point was measured.

The in vitro Release Behavior of HA-CD@DOX & Fc^{+}-C_{18}@CUR BNs

To verify the pH- and GSH-responsive release behavior of the HA-CD@DOX & Fc^{+}-C_{18}@CUR BNs in the TME, the release medium with different pH and GSH concentrations was set up, including a series of acid medium (pH 5.5, pH 6.5 and pH 7.4 PBS solution) and a series of GSH solution (0 mM, 5 mM and 20 mM GSH in pH 6.5 PBS solution). A precision amount of 1 mL HA-CD@DOX & Fc^{+}-C_{18}@CUR solution was placed in a dialysis bag within the above release medium, shaking at a constant temperature of 37 °C and 100 rpm. Samples from release medium were taken at predetermined time points (0, 2, 4, 6, 8, 10, 12, 24, and 48 h) to measure and calculate the cumulative release of DOX and CUR.

The Anti-Tumor Synergy Evaluation of DOX and CUR

4T1 mouse breast cancer cell was selected as research object to verify the anti-tumor synergistic effects of DOX and CUR by the MTT assay. The combination index (CI) was used to analyze the drug interactions, and the equation was displayed as follows.

$$CI = \frac{D1}{Dx1} + \frac{D2}{Dx2} \quad (1)$$

D1 and D2 refer to the concentrations of the two drugs when the growth inhibition rate reaches X under the combination treatment. While Dx1 and Dx2 refer to the concentrations of the two drugs when the growth inhibition rate reaches X when the two drugs are used monotherapy. When CI < 1, it indicates that the two drugs have a synergistic effect.

Briefly, cells were seeded into 96-well plates and incubated for 24 h. Then, medium was substituted by a series of DOX, CUR and DOX+CUR solutions with different concentrations, and cultured for another 24 h. According to the instructions of MTT kit (KeyGene, China), the cell viability was measured.

The Cytotoxicity Assay of HA-CD@DOX & Fc^{+}-C_{18}@CUR BNs

4T1 mouse breast cancer cells and LO2 human normal hepatocytes were selected as research objects to detect the cytotoxicity of different preparations. 4T1 and LO2 cells were purchased from the Cell Bank of Chinese Academy of Sciences (Shanghai, China). And the MTT assay was divided into four groups, including HA-CD & Fc^{+}-C_{18} group, free DOX & CUR group, HA-CD@DOX & Fc^{+}-C_{18} group and HA-CD@DOX & Fc^{+}-C_{18}@CUR group. The MTT assay was performed as described as above, and the cell viability was calculated as following equation.

$$\text{Cell viability}\,(\%)=\frac{\text{ODs}-\text{ODb}}{\text{ODc}-\text{ODb}}\times 100\% \tag{2}$$

ODs refer to the absorbance value of cells in experimental groups, ODc refers to the absorbance value of cells in blank groups, and ODb refers to the absorbance value of the zero setting groups.

Cellular Uptake and Tumor-Targeted Behavior of HA-CD@DOX & Fc^{+}-C_{18}@CUR BNs

4T1 cells were selected as research objects, and the cellular uptake efficiency was qualitatively and quantificationally evaluated by confocal laser scanning microscope (CLSM) and flow cytometry (FCM). The uptake evaluation was divided into three groups, including HA-CD@DOX group, HA-CD@DOX & Fc^{+}-C_{18}@CUR group, and HA + HA-CD@DOX & Fc^{+}-C_{18}@CUR group, and each group was further divided into three time points (1, 2, 4 h). In HA + HA-CD@DOX & Fc^{+}-C_{18}@CUR group, cells were pretreated with HA for 1 h to block the CD44 receptor.

First, cells were seeded, then were treated with different preparations separately at a preset time. After incubation, cells were fixed with 4% paraformaldehyde and stained by nuclear dye (Hoechst 33342, 10 μg/mL). Detected by CLSM, the images showed the distribution of DOX in cells. Second, for FCM analysis, cells were seeded. After treated respectively, cells were digested and then resuspended in PBS for sample loading. All the above operations should be carefully shielded from light.

In addition, to further explore the tumor cell targeting of the HA-CD@DOX & Fc^{+}-C_{18}@CUR, the cellular uptake behavior of 4T1 cells and LO2 cells at different time points was compared by FCM. The experimental procedures were the same as above.

In vivo Distribution of HA-CD@DOX & Fc^{+}-C_{18}@CUR BNs

All animal procedures were performed in accordance with the Guidelines for Care and Use of Laboratory Animals of China Pharmaceutical University and approved by the Animal Management and Ethics Committee of China Pharmaceutical University (Nanjing, China). To establish tumor-bearing mouse models, 1×10^{7} 4T1 cells were subcutaneously injected into armpit of BALB/c mice. When the tumor volume reached about 200 mm^{3}, free DOX + CUR, HA-CD@DOX & Fc^{+}-C_{18}, and HA-CD@DOX & Fc^{+}-C_{18}@CUR were separately injected into the tail vein in a volume of 200 μL per mouse. 24 h after administration, the mice were sacrificed, of which the heart, liver, spleen, lung, kidney and tumor were isolated and washed for fluorescence imaging.

In vivo Antitumor Evaluation and Biocompatibility Assessment of HA-CD@DOX & Fc^{+}-C_{18}@CUR BNs

The tumor-bearing mice were randomly divided into four groups (n = 5), including saline group, free DOX + CUR group, HA-CD@DOX & Fc^{+}-C_{18} group, and HA-CD@DOX & Fc^{+}-C_{18}@CUR group. The mice were intravenously

administered saline, free DOX + CUR, HA-CD@DOX & Fc^{+}-C_{18}, and HA-CD@DOX & Fc^{+}-C_{18}@CUR (5 mg/kg for DOX) every two days for five times, respectively. During the administration process, the tumor volume and body weight of each mouse were recorded every day.

For in vivo antitumor evaluation, mice were sacrificed; then, the tumors were collected and photographed. Subsequently, tumors were fixed with formalin solution for 48 h, and then were analyzed for H&E, Ki67 and Tunel staining. For in vivo biocompatibility assessment, the heart, liver, spleen, lung and kidney were collected, and analyzed for H&E staining after fixation.

Statistical Analysis

All results were presented as mean ± SD statistical analysis from at least three independent experiments. A two-tailed *t*-test was performed, and ***$p < 0.001$, **$p < 0.01$ and *$p < 0.05$ were considered statistically significant.

Results and Discussion

Preparation and Characterization of HA-CD@DOX

Firstly, the synthesized HA-CD was validated by ^{1}H-NMR (Figure S1). By comparing the differences among the results of HA, *β*-CD and HA-CD, new peaks appeared in the 1.34–1.50 ppm range in HA-CD, which were attributed to -NH- and -CH- on hexamethylene diamine. In addition, the characteristic peaks of HA and *β*-CD still existed in the nuclear magnetic map of HA-CD. The above results proved the successful graft of *β*-CD onto the HA chains.

The HA-CD@DOX obtained by the host–guest interaction was verified by FTIR (Figure 1A) and DSC (Figure 1B). In the infrared spectrum of HA-CD@DOX, the characteristic peak of DOX at 806 cm^{-1} disappeared, which is caused by the vibration on the benzene ring. The characteristic peaks of DOX and HA-CD were not present at 1570 cm^{-1}. However, the infrared spectrum of the physical mixture retained almost all the characteristic peaks of DOX and HA-CD. Therefore,

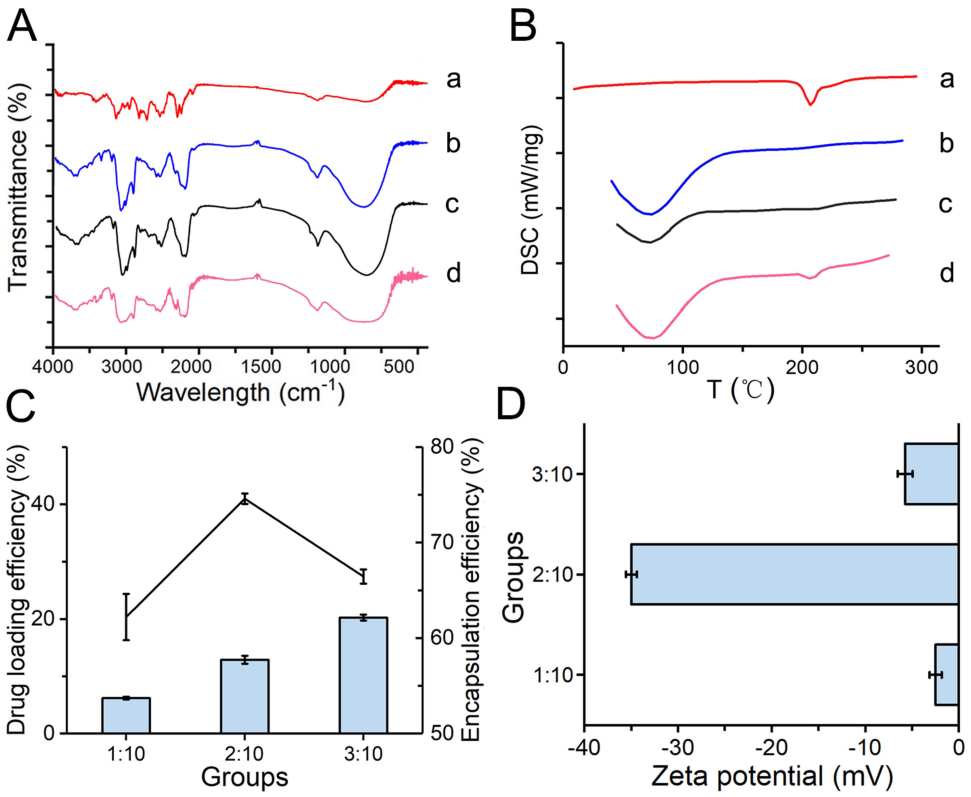

Figure 1 The preparation and characterization of HA-CD@DOX: (**A**) FTIR and (**B**) DSC plot of HA-CA@DOX (a refers to DOX, b refers to HA-CD, c refers to HA-CD @DOX, and d refers to the physical mixture of DOX and HA-CD). (**C**) Drug loading efficiency and encapsulation efficiency and (**D**) Zeta potential of three formulations with different mass ratio between DOX and HA-CD.

HA-CD@DOX differs from a simple physical mixture and actually forms an inclusion complex. Based on the disappearance and partial attenuation of the characteristic peak of benzene ring in DOX, it can be speculated that the inclusion site of DOX with the cyclodextrin cavity may be the hydrophobic anthracene ring. In addition, DSC plot showed that DOX had an endothermic peak at 217 °C, which was the melting point of DOX, while HA-CD had an endothermic peak at 75 °C. The DSC map of the physical mixture was a superposition that included DOX and HA-CD maps, but HA-CD@DOX completely displayed a new curve with a different peak type and location, indicating the formation of inclusion complexes and thus a new phase.

The encapsulation efficiency and drug loading efficiency of HA-CD@DOX with different formulations are shown in Figure 1C. With the rise of DOX adding ratio, the drug loading continued to increase, indicating that the cavity of HA-CD had a strong loading capacity. Due to the hydrophobicity of the cavity in CD, it can spontaneously associate with the hydrophobic DOX after desalting, forming host-guest complexes. Referring to the corresponding potential values of the three preparations (Figure 1D), the lowest potential value was found when the mass ratio of DOX to HA-CD was 2:10, which was conductive to its stability during circulation in vivo. In summary, the formation of HA-CD@DOX was confirmed by FTIR and DSC. Considering the drug loading efficiency and zeta potential, the optimal mass ratio of DOX to HA-CD was determined to be 2:10.

Preparation and Characterization of Fc^{+}-C_{18}@CUR Micelles

Firstly, the synthesized Fc-C_{18} was validated by ^{1}H-NMR (Figure S2). In the plot of Fc-C_{18}, the characteristic peak of carboxyl hydrogen in Fc disappeared at 12.18 ppm, and the characteristic peak of methyl hydrogen of C_{18} and cyclopentadienyl hydrogen of Fc appeared simultaneously, indicating the successful synthesis of Fc-C_{18}.

Fc is hydrophilic in the oxidized state and hydrophobic in the reduced state, and the transition between hydrophilicity and hydrophobicity can be achieved by redox reactions. Taking this property, the amphiphilic Fc^{+}-C_{18} can be obtained by oxidation of Fc-C_{18}. Therefore, Fc^{+}-C_{18} could self-assemble into micellar particles with a hydrophobic inner cavity. When the infrared beam irradiated the solution, a distinct light column appeared due to the "Tyndall effect" of the micelles, as shown in Figure 2A. The particle size distribution of the blank micelles is shown in Figure 2B, where the average particle size of blank micelles was 267 nm and PDI was less than 0.3, which meets the needs of nano-antitumor drug delivery carriers. In addition, the CMC concentration of Fc^{+}-C_{18} micelle solution was 0.02 mg/mL determined by pyrene fluorescent probe method, as shown in Figure S3. In the curve, I_3 presented the fluorescent intensity of the pyrene association complex, while I_1 presented that of the pyrene monomer. The I_3/ I_1 value was stable in the initial phase and gradually increased as the micelle formed, with the turning point being the CMC value. A smaller CMC value facilitated the stability of the micelles during systemic circulation and avoided premature leakage of the encapsulated drug, thereby reducing the toxic side effects of the drug.

Similarly, three groups of different CUR addition ratios were set to investigate the encapsulation efficiency, drug loading efficiency, and particle size of the resulting prescription, as shown in Figure 2C and D. The average particle size of the Fc^{+}-C_{18}@CUR micelles increased with increasing CUR mass, which may be due to the relatively loose arrangement of hydrophobic core in the micelles with higher drug loading, leading to a large particle size. Comprehensively, when the mass ratio of CUR and Fc^{+}-C_{18} was 1:6, the particle size of Fc^{+}-C_{18}@CUR micelles was more in line with the requirements of the nano-drug delivery system.

Preparation and Characterization of HA-CD@DOX & Fc^{+}-C_{18}@CUR BNs

The results of particle size and zeta potential of different concentration ratios of HA-CD@DOX & Fc^{+}-C_{18}@CUR are shown in Figure 3A and B. The HA chains were negatively charged owing to the abundant carboxyl groups, while Fc^{+}-C_{18} belonged to cationic micelles and were positively charged. Hence, when HA-CD@DOX and Fc^{+}-C_{18}@CUR were mixed, they were automatically assembled by electrostatic interaction to form "micelle core-HA shell" nanoparticles. According to the trend of particle size and potential, an interesting phenomenon could be found that the increase of HA failed to increase the coat thickness of micelle particles. After HA coating, the particle size of nanoparticles increased, but the potential was significantly reversed. The formed BNs contained only one micellar core with a limited HA coating thickness, which was attributed to limited electrostatic interactions. Therefore, we finally selected nanoparticles with

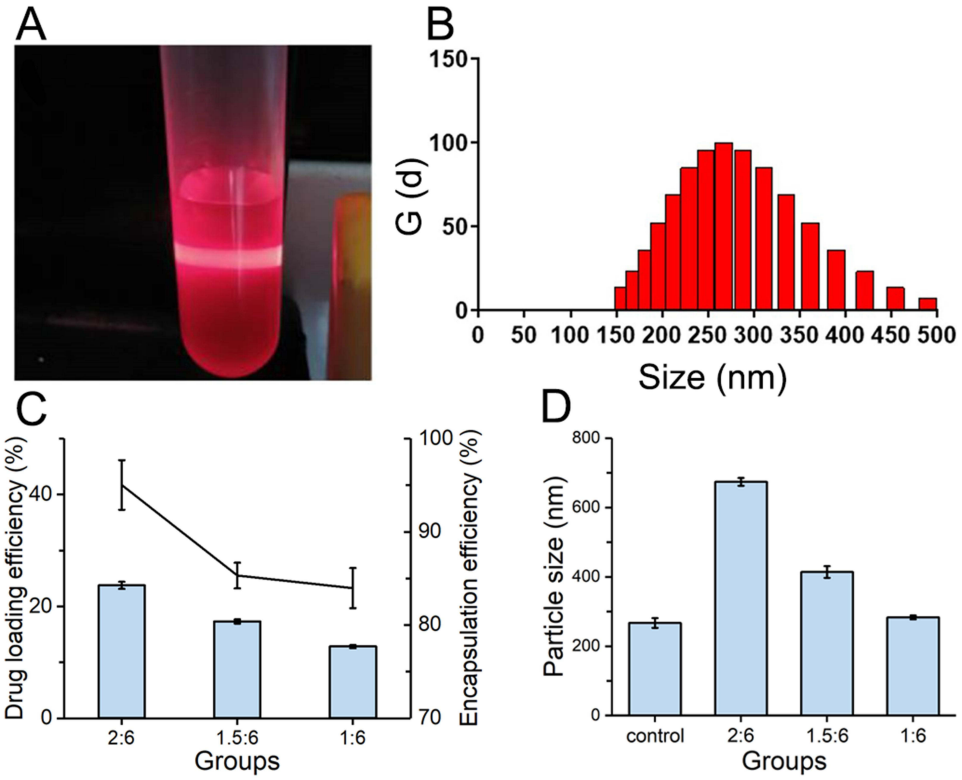

Figure 2 The preparation and characterization of Fc^{+}-C_{18}@CUR: (**A**) Tyndall effect and (**B**) particle size of blank Fc^{+}-C_{18} micelle particles. (**C**) Drug loading efficiency and encapsulation efficiency and (**D**) particle size of three formulations with different mass ratio between CUR and Fc^{+}-C_{18}.

a concentration ratio of 1:1, which had a particle size of 299 ± 15.17 nm. The morphology of HA-CD@@DOX & Fc^{+}-C_{18}@CUR BNs are displayed in Figure 3C. The laminated drug-loaded nanoparticles exhibited a smooth spherical structure with uniform size. Furthermore, placed at 4°C for 120 h, the particle size changes of BNs with times were recorded in Figure 3D. With the extension of the storage time, the particle size increased slightly from 300 to 350 nm, of which the growth rate was slow, confirming the excellent stability. At least for 5 days, the HA-CD@DOX & Fc^{+}-C_{18} @CUR BNs are able to maintain a relatively stable state at 4°C.

The in vitro Release Behavior of HA-CD@DOX & Fc^{+}-C_{18}@CUR BNs

The release curves of DOX and CUR in nanoparticles at different pH are shown in Figure 4A and B, respectively. The cumulative release of both drugs was highest at pH 5.5 and the least at pH 7.4, showing significant pH-dependence. The pH-responsive release behavior could be explained by the fact that the amide bonds on the HA chains gradually hydrolyzed in the acidic environment, leading to the shedding of DOX-loaded *β*-CD. However, the maximum cumulative release of DOX within 48 h was only about 40%, which may be due to the fact that DOX was encapsulated in the cavity of *β*-CD, slowing down its release rate. Similarly, the release of CUR also increased with decreasing pH, presumably due to the decreased steric binding of HA chains to micelles, resulting in more easy diffusion of CUR from micellar particles.

Moreover, the release behaviors of nanoparticles in GSH conditions are displayed in Figure 4C and D. The cumulative release of DOX and CUR at reducing environment was much greater than that at non-reducing environment, and the release behavior was accelerated with the increase of GSH concentration, exhibiting obvious GSH-responsive. In GSH conditions, Fc^{+} groups were reduced to Fc groups, changing from hydrophily to hydrophobicity, and the amphiphilic structure was disrupted, leading to the disintegration of the core micelle. The TEM of HA-CD@DOX & Fc^{+}-C_{18}@CUR BNs in 20 mM GSH solutions is shown in Figure S4, where the structure of nanoparticles was destroyed and irregular floccule was formed. Simultaneously, orange floccule could also be seen in the appearance of the solution. Noticeably, reduced Fc groups were prone to interact with *β*-CD through hydrophobic effect,[35–37] and competed for DOX

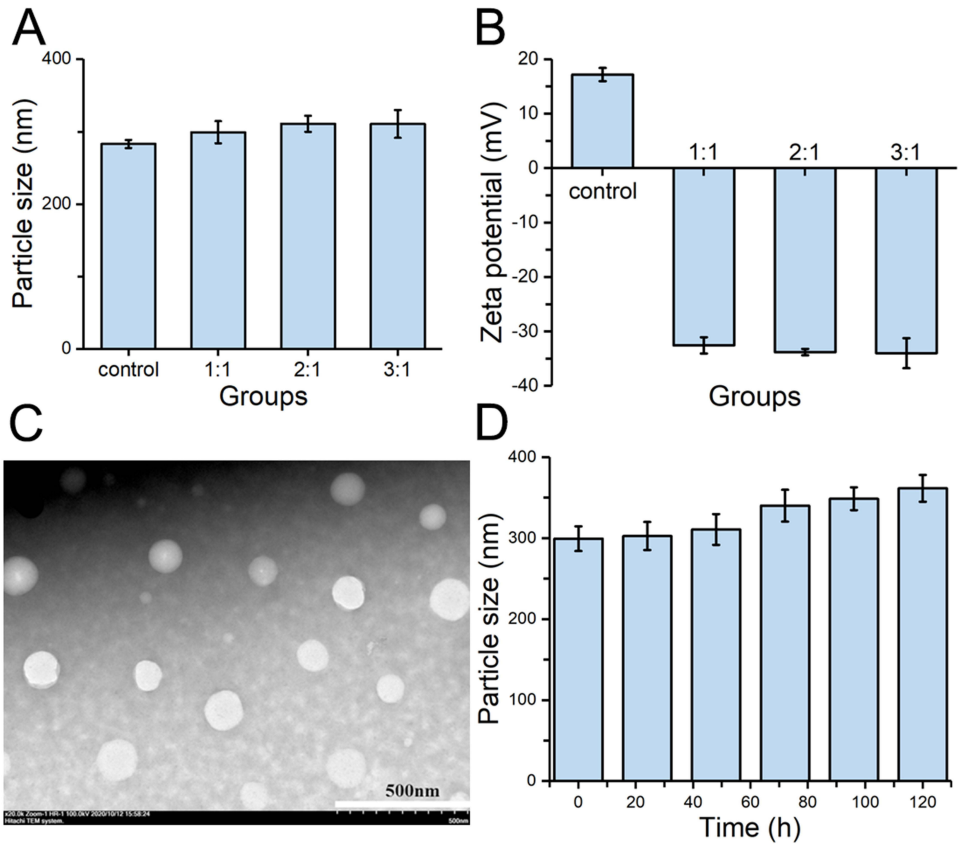

Figure 3 The preparation and characterization of HA-CD@DOX & Fc^{+}-C_{18}@CUR BNs: (**A**) Particle size and (**B**) Zeta potential of nanoparticles in different formulations. (**C**) TEM image of the final HA-CD@DOX & Fc^{+}-C_{18}@CUR BNs. (**D**) The trend of particle size over time storing at 4°C for 120 h.

binding sites, which could explain why GSH also accelerated DOX release. Different layers have different cargoes and responded to different stimuli, cooperatively constructing complex drug release behavior. Comprehensively, BNs displayed different in vitro drug release behavior under different media conditions, proving the pH- and GSH- responsive release properties. This property allowed nanoparticles to remain stable in the blood circulation, and once they reach the tumor sites, they could response to TME, achieving faster drug release and higher antitumor effects.

The Antitumor Effects of HA-CD@DOX & Fc^{+}-C_{18}@CUR BNs

The synergistic antitumor effects between DOX and CUR were investigated in 4T1 cell models, and the cytotoxicity of free DOX, free CUR and mixture of the two (c/c = 1:1) is shown in Figure 5A. CUR owned relative biosafety, in which 10 μg/mL still resulted in cell viability of more than 80%, while the cytotoxicity of DOX was significantly enhanced with increasing concentration. At concentrations up to 5 μg/mL, the cytotoxicity of the mixture was more pronounced than that of either alone. For further calculation of the IC_{50} values revealed an IC_{50} of 5.438 μg/mL for DOX, 658 μg/mL for CUR, and 4.305 μg/mL for the mixture of DOX and CUR. Then the interactions between DOX and CUR were judged according to the CI. Herein, the CI value was 0.40, which was less than 1, indicating that DOX combined with CUR had synergistic antitumor effects. This phenomenon may be due to the effective inhibition of DOX MDR by CUR, hence improving stronger tumor cell-killing effect.

In addition, taking 4T1 cells and LO2 cells as investigation object, the cytotoxicity of HA-CD & Fc^{+}-C_{18} (empty vectors), HA-CD@DOX & Fc^{+}-C_{18} (final preparations without CUR), HA-CD@DOX & Fc^{+}-C_{18}@CUR (final preparations), and DOX + CUR (free drugs) was evaluated, and the results are displayed in Figure 5B and C, respectively. First, the survival rates of cells incubated with empty vectors were above 80% within the concentration range set in experiments, proving the high safety and excellent biocompatibility of this ideal delivery carrier for antitumor drugs.

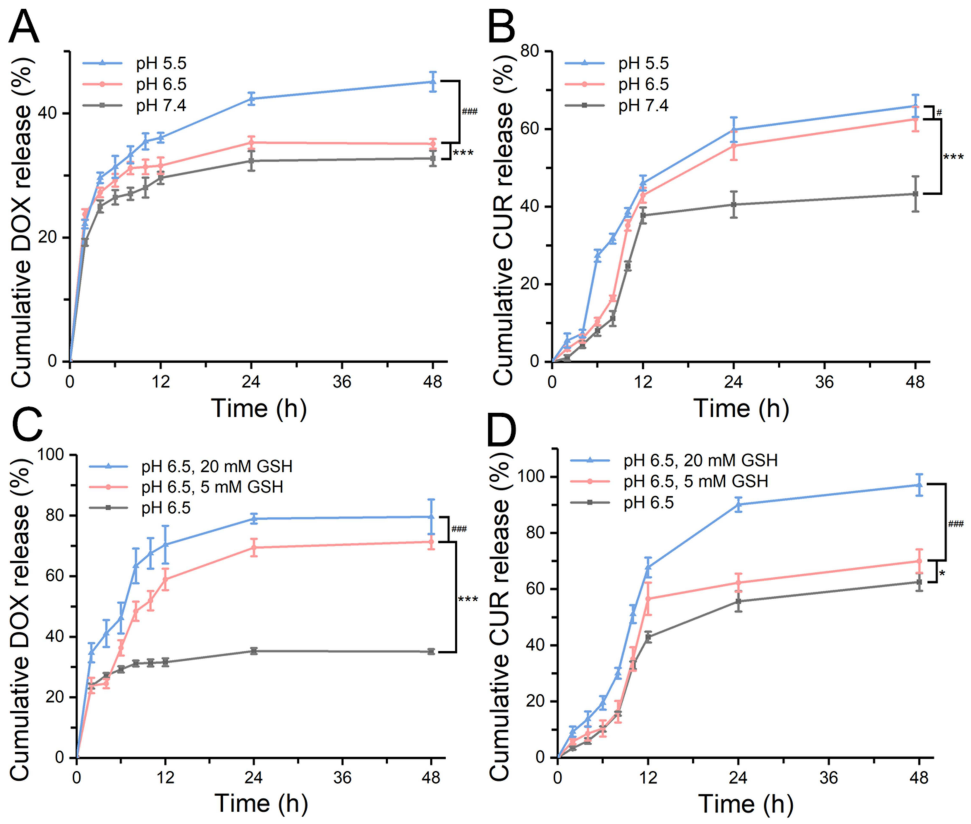

Figure 4 The release curves of nanoparticles in different media: Cumulative release rate of (**A**) DOX and (**B**) CUR in media with different pH (pH 5.5, 6.5 and 7.4). Cumulative release rate of (**C**) DOX and (**D**) CUR in media with different GSH concentration (0, 5, and 20 mM). Statistical significance: *p<0.05, ***p<0.001, #p<0.05 and ####p<0.001.

Analysis of the MTT results of 4T1 cells showed that the cytotoxicity of drug-containing groups was concentration-dependent. As concentration exceeded 1.25 μg/mL, HA-CD@DOX & Fc^{+}-C_{18}@CUR showed stronger killing effect on tumor cells than HA-CD@DOX & Fc^{+}-C_{18}, reflecting the synergistic effects of combined drugs. Moreover, when concentration of DOX was higher than 0.625 μg/mL, more effective cytotoxic effects were observed in HA-CD @DOX & Fc^{+}-C_{18}@CUR groups than that of free drugs. The IC_{50} value of DOX +CUR, HA-CD@DOX & Fc^{+}-C18 @CUR were 4.305 and 2.553 μg/mL, respectively. The superior antitumor effects of HA-CD@DOX & Fc^{+}-C_{18}@CUR BNs could be attributed to the following two reasons: (1) nanoparticles actively targeted the CD44 receptors, and CD44-mediated cellular internalization was more efficient than free diffusion. (2) acidic and reducing TME accelerated the release of DOX and CUR, thereby promoting the synergism.

As for the results of LO2 cells, when compared with 4T1, HA-CD@DOX & Fc^{+}-C_{18}@CUR consistently performed weaker cell-killing effects than free drugs, and were less toxic to LO2 cells. LO2 cells, as normal cells, had low CD44 expression and a lower uptake rate of HA-CD@DOX & Fc^{+}-C_{18}@CUR BNs than free drugs. Simultaneously, the concentrations of H^{+} and GSH in normal cells were extremely low, resulting in a significant reduction in drug release and a weak inhibitory effect on cells. In summary, HA-CD@DOX & Fc^{+}-C_{18}@CUR BNs are an efficient tumor-targeted drug delivery systems that exert the synergistic effects of DOX and CUR with favorable tumor-responsive drug release behavior.

The Cellular Uptake Efficiency of HA-CD@DOX & Fc^{+}-C_{18}@CUR BNs

The cellular uptake behaviors were qualitatively evaluated by CLSM, and the images are displayed in Figure 6A–C. The rate of cellular internalization was more significant for HA-CD@DOX & Fc^{+}-C_{18}@CUR BNs, compared to HA-CD @DOX at the same incubation time. This phenomenon could be attributed to the regular spherical structure of nanoparticles, while the shape of HA-CD@DOX may be a non-spherical structure formed by the winding of macromolecular HA chains, which resulted in reducing the endocytosis and cellular uptake.[38] Moreover, the cellular uptake

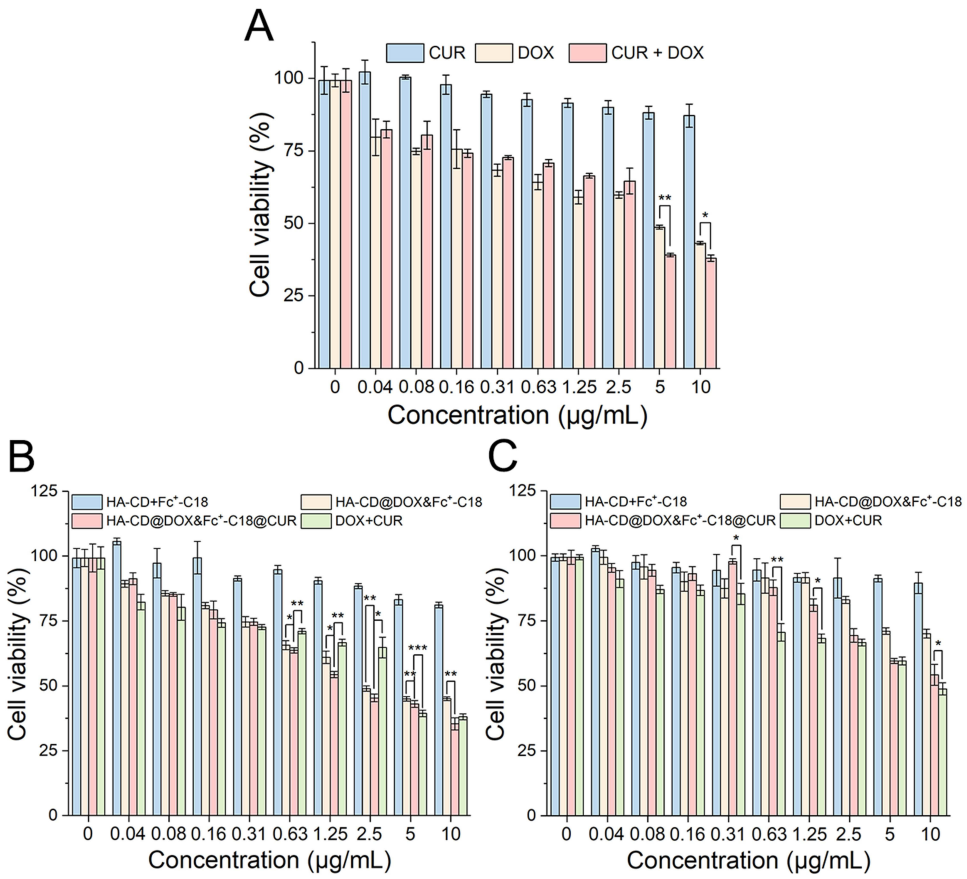

Figure 5 The cytotoxicity evaluation of HA-CD@DOX & Fc^{+}-C_{18}@CUR BNs: (**A**) The investigation of synergistic effects of DOX and CUR. The cell viabilities of different preparations on (**B**) 4T1 cells and (**C**) LO2 cells. Statistical significance: *p<0.05, **p<0.01 and ***p<0.001.

efficiency of nanoparticles was obviously decreased after HA pretreatment. The free HA blocked the CD44 receptors on cell surfaces, and limited the binding of nanoparticles to the receptors, thereby impeding CD44-mediated endocytosis behavior. Next, the quantitative investigation of cellular internalization is exhibited in Figure 6D–F, and the statistical graphs are shown in Figure 6G–I. The results were consistent with those described above, again confirming the efficient CD44-mediated endocytosis behavior of HA-CD@DOX & Fc^{+}-C_{18}@CUR BNs.

Furthermore, the difference in nanoparticles uptake between cancer cells and normal cells was also demonstrated, and the results were shown in Figure S5. The fluorescence intensity of LO2 cells was much lower than that of 4T1 cells after incubation for 1, 2 and 4 h, and there was no significant change in the fluorescence intensity of LO2 cells with the extension of incubation time. The uptake behavior of nanoparticles was mediated by CD44 receptor, which yet significantly low-expressed on the surface of normal cells. Taken together, it is proved that HA-CD@DOX & Fc^{+}-C_{18}@CUR BNs could be actively targeted to tumor cells and achieve rapid drug release at specific sites under the special TME.

In vivo Distribution and Antitumor Evaluation of HA-CD@DOX & Fc^{+}-C_{18}@CUR BNs

The in vivo distribution results after DOX+CUR and HA-CD@DOX & Fc^{+}-C_{18}@CUR treatment, respectively, are shown in Figure 7A. In DOX+CUR groups, the fluorescence of liver and kidney was strong, confirming that DOX was easily removed by rapid metabolism after entering the systemic circulation. While in HA-CD@DOX & Fc^{+}-C_{18}@CUR group, the fluorescence intensity of kidney decreased, indicating that the amount of DOX metabolism reduced. Moreover, the accumulation of HA-CD@DOX & Fc^{+}-C_{18}@CUR in tumor tissue was significantly higher than that of free drugs. The results of imaging illustrated that HA-CD@DOX & Fc^{+}-C_{18}@CUR prolonged DOX circulation in vivo and improved DOX targeting to tumor tissues. The outer layer of BNs was coated with HA, which facilitated the prolongation of systemic circulation and efficient targeting to the tumor site, thus enhancing drug accumulation in the tumor.

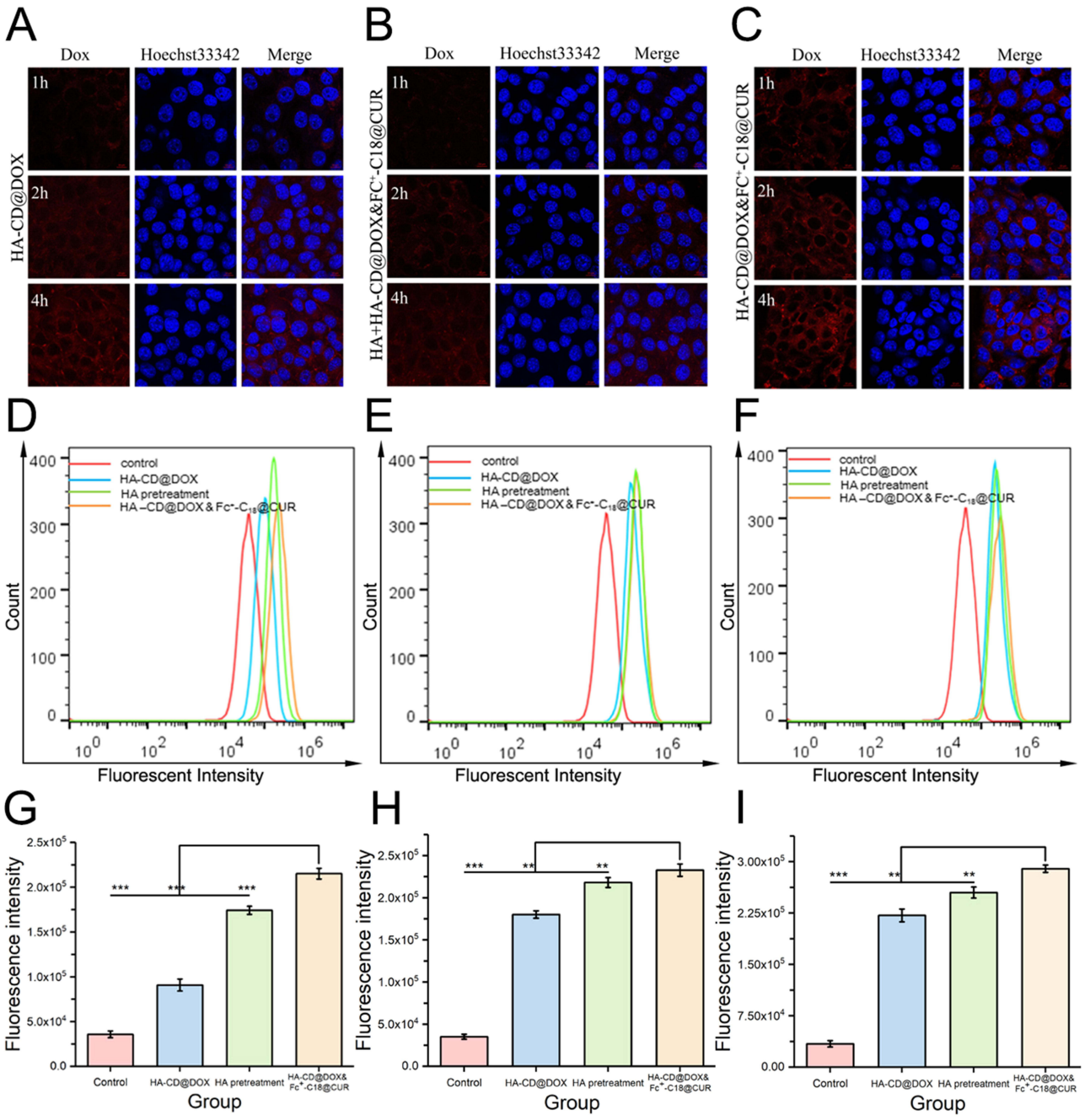

Figure 6 The cellular uptake behavior of HA-CD@DOX & Fc^{+}-C_{18}@CUR BNs: (**A**–**C**) The CLSM images and (**D**–**F**) the FCM results of 4T1 cells after respectively incubation with HA-CD@DOX, HA-CD@DOX & Fc^{+}-C_{18}@CUR along with HA pretreatment, and HA-CD@DOX & Fc^{+}-C_{18}@CUR for 1, 2 and 4 h. (**G**–**I**) The statistical graphs corresponding to the FCM results. Statistical significance: **p<0.01 and ***p<0.001.

In the mouse tumor models, the changes in body weight and tumor volume were continuously monitored within 10 days of administration, and the results are shown in Figure 7B and C, respectively. The tumor growth rate of the saline group was the fastest, which was twice that of HA-CD@DOX & Fc^{+}-C_{18}@CUR group. The free drugs also exhibited a certain tumor inhibition effect, but also showed strong systemic side effects, leading to a weight loss of about 27%. However, the body weight of the HA-CD@DOX & Fc^{+}-C_{18} group and HA-CD@DOX & Fc^{+}-C_{18}@CUR group separately decreased by 12% and 6%, significantly reducing the DOX-induced toxicity, and the presence of CUR further improved the safety, which could be owing to the tissue protective effect of CUR. Subsequently, we sacrificed and dissected the tumor tissues of the mice, which and their weights are shown in Figure 7D and E. Compared with the saline

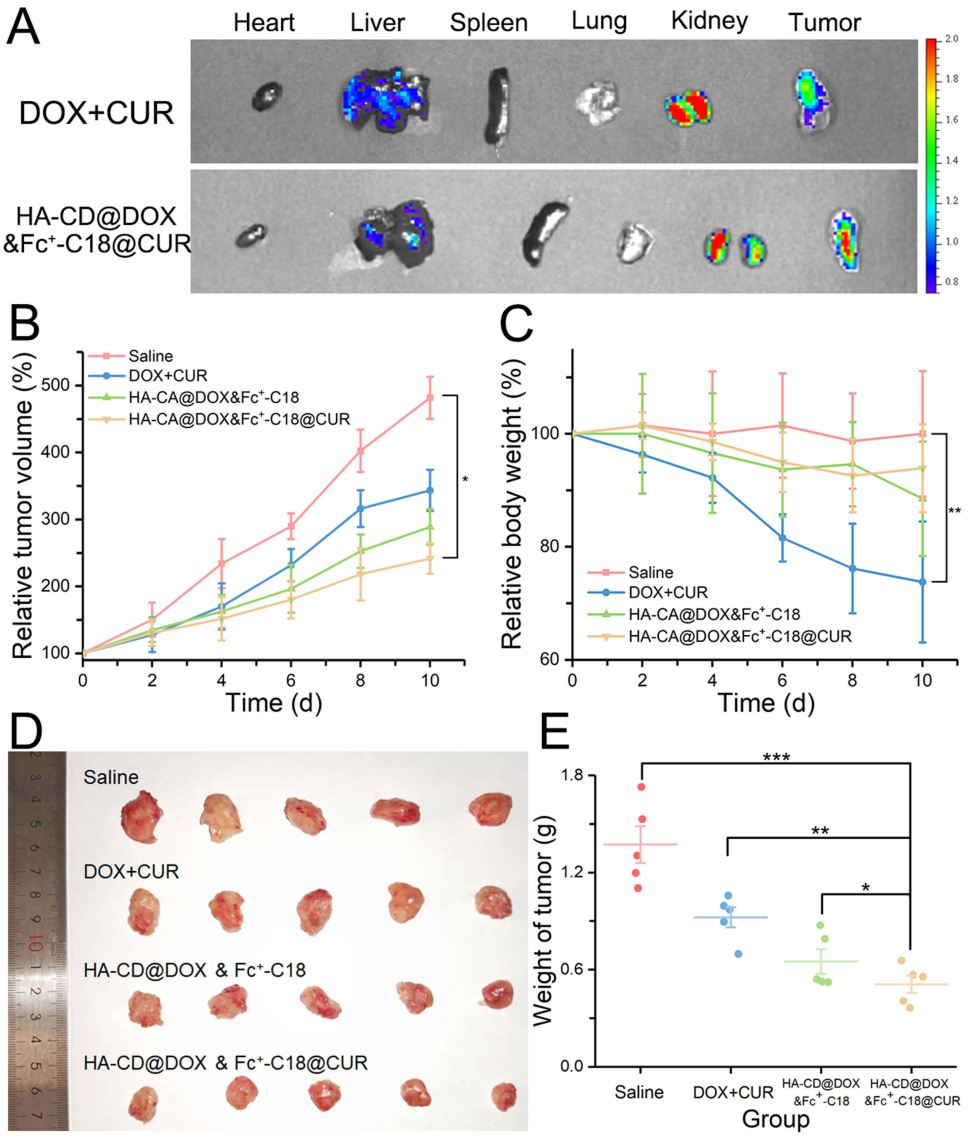

Figure 7 In vivo distribution and antitumor effects of HA-CD@DOX & Fc^{+}-C_{18}@CUR BNs: (**A**) The ex vivo images indicating the accumulation of free DOX+CUR and HA-CD@DOX & Fc^{+}-C_{18}@CUR within the tumor and other organs after 24 h treatment. The relative (**B**) tumor volume and (**C**) body weight changes of mice during the treatment period after injection treatments. (**D**) The representative photograph of tumors dissected, and (**E**) statistical graph of tumor weight in different groups. Statistical significance: *p<0.05, **p<0.01 and ***p<0.001.

group, tumor inhibition rates of DOX+CUR, HA-CD@DOX & Fc^{+}-C_{18} and HA-CD@DOX & Fc^{+}-C_{18}@CUR group were 32.8%, 52.6% and 62.9%, respectively. The admirable antitumor effects of HA-CD@DOX & Fc^{+}-C_{18}@CUR BNs were related to their active tumor-targeting and synergistic chemotherapy effects.

Additionally, the significant inhibition of HA-CD@DOX & Fc^{+}-C_{18}@CUR BNs on tumor growth was further confirmed by H&E, Ki67 and Tunel staining, as shown in Figure 8A. In the H&E images, the tumor cells in the saline group were closely arranged and in good growth state, with deep nuclear staining and less cytoplasm, which were consistent with typical tumor histopathological characteristics. However, there were different degrees of tumor tissue necrosis in experimental groups, indicating the proapoptotic effects on tumor cells. Among them, cells treated with HA-CD@DOX & Fc^{+}-C_{18}@CUR BNs were the most loosely arranged, the intercellular space was significantly enlarged, and the area of tissue necrosis was the largest, exhibiting the best antitumor effect. In Ki67 imaging, Ki67 protein is widely expressed in proliferating cells, closely related to mitosis, and can be used as a marker of proliferating cells. The expression of Ki67 protein in the control group was the highest, that is, the yellow staining was the most. After drug

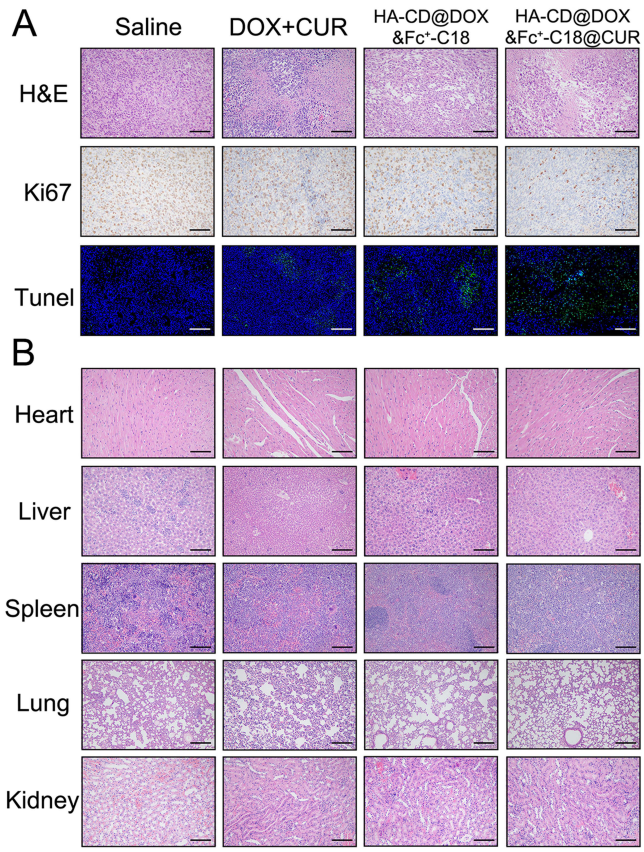

Figure 8 Histopathologic examination of tumor tissues and major organs: (**A**) The H&E, Ki 67 and Tunel staining of tumor tissue after treatment with saline, DOX+CUR, HA-CD@DOX & Fc^{+}-C_{18} and HA-CD@DOX & Fc^{+}-C_{18}@CUR, respectively. (**B**) The H&E staining of major organs after treatment with saline, DOX+CUR, HA-CD @DOX & Fc^{+}-C_{18} and HA-CD@DOX & Fc^{+}-C_{18}@CUR, respectively.

administration, the expression of Ki67 was downregulated, and the cell positive rate was the lowest in HA-CD@DOX & Fc^{+}-C_{18}@CUR group. Furthermore, the Tunel assay could distinguish apoptotic cells from normal cells by detecting the fragmentation of nuclear DNA during apoptosis. Therefore, in the Tunel results, the green fluorescence intensity in the four groups increased sequentially, with HA-CD@DOX & Fc^{+}-C_{18}@CUR representing the strongest antitumor efficacy.

Subsequently, the safety of HA-CD@DOX & Fc^{+}-C_{18}@CUR BNs was investigated by histological analysis of major organs, including heart, liver, spleen, lung and kidney, as shown in Figure 8B. In particular, free DOX was highly cardiotoxic, while its toxicity was significantly decreased upon encapsulation with the preparations. Moreover, CUR further reduced the cardiotoxicity of DOX and exerted an excellent protective effect. CUR showed multitargeting capabilities against cancer cells, but low toxicity in normal healthy cells, that is, selective toxicity.[39] No obvious pathological features were observed in the sections of other organs, proving that HA-CD@DOX & Fc^{+}-C_{18}@CUR BNs could effectively improve the biological safety and reduce systemic toxic side effects.

Conclusion

In summary, we have successfully established a bilayer "shell-core" nanoparticle, capable of modulating the TME through multiple stimulus responses for multi-drug delivery of combination chemotherapy. The HA-CD@DOX & Fc^{+}-C_{18}@CUR BNs are composed of a "shell-core" structure, with an outer layer of DOX-loaded HA-CD, and an inner layer of CUR-loaded Fc^{+}-C_{18} micelles. This nanodrug delivery system provides more drug loading sites and greatly improves the stability of drugs. HA encapsulation allows the nanoparticles to circulate in vivo for a longer time, and CD44-mediated active targeting enhances drug accumulation in tumor sites. Moreover, HA-CD can respond to the slight acidity in TME, accelerating the release of DOX at tumor site. The micelle structure is GSH-responsive, and reverses hydrophilic and hydrophobic in TME, leading to micelle cleavage and CUR release. The isolated Fc groups compete for

the CD cavity and further promote DOX release. The morphology and excellent responsive drug release behavior of HA-CD@DOX & Fc^{+}-C_{18}@CUR BNs were confirmed experimentally. In addition, their synergistic antitumor effects and efficient tumor targeting were verified at cellular level. Finally, we constructed reliable animal models and observed effective tumor targeting behavior and significant tumor cytotoxicity with high biosafety in tumor-bearing mice. HA-CD @DOX & Fc^{+}-C_{18}@CUR BNs respond to and modulate TME, and exert the synergistic anti-tumor effect of DOX and CUR, including enhancing tumor targeting cell-killing effect and reducing toxicity to normal tissues. Furthermore, the bilayer nanoparticle structures also provided a promising delivery platform for combination chemotherapy in cancer therapy, where more chemotherapeutic agents could be delivered in combinations with high efficiency. Altogether, this "shell-core" nanoparticle is an admirable drug delivery system for TME modulation and combination chemotherapy.

Disclosure

The authors report no conflicts of interest in this work.

References

1. Gong Z, Liu X, Zhou B, et al. Tumor acidic microenvironment-induced drug release of RGD peptide nanoparticles for cellular uptake and cancer therapy. *Biointerfaces*. 2021;202:1. doi:10.1016/j.colsurfb.2021.111673
2. Yang M, Li J, Gu P, et al. The application of nanoparticles in cancer immunotherapy: targeting tumor microenvironment. *Bioact Mater*. 2021;6 (7):1973–1987. doi:10.1016/j.bioactmat.2020.12.010
3. Xiao Y, Yu D. Tumor microenvironment as a therapeutic target in cancer. *Pharmacol Ther*. 2021;221:4. doi:10.1016/j.pharmthera.2020.107753
4. Wu T, Dai Y. Tumor microenvironment and therapeutic response. *Cancer Lett*. 2017;387:61–68.
5. Hanahan D, Weinberg RA. Hallmarks of cancer: the next generation. *Cell*. 2011;144:646–674.
6. Thakkar S, Sharma D, Kalia K, et al. Tumor microenvironment targeted nanotherapeutics for cancer therapy and diagnosis: a review. *Acta Biomater*. 2020;101:43–68.
7. Qu Y, Chu BY, Wei XW, et al. Redox/pH dual-stimuli responsive camptothecin prodrug nanogels for "on-demand" drug delivery. *J Control Release*. 2019;296:93–106.
8. Li H-J, Du J-Z, Liu J, et al. Smart superstructures with ultrahigh pH-sensitivity for targeting acidic tumor microenvironment: instantaneous size switching and improved tumor penetration. *Acs Nano*. 2016;10:6753–6761.
9. Yang Z, Fan W, Tang W, et al. Near-infrared semiconducting polymer brush and ph/gsh-responsive polyoxometalate cluster hybrid platform for enhanced tumor-specific phototheranostics. *Angew Chem Int Ed*. 2018;57:14101–14105.
10. Khawar IA, Kim JH, Kuh H-J. Improving drug delivery to solid tumors: priming the tumor microenvironment. *J Control Release*. 2015;201:78–89. doi:10.1016/j.jconrel.2014.12.018
11. Liu T, Han C, Wang S, et al. Cancer-associated fibroblasts: an emerging target of anti-cancer immunotherapy. *J Hematol Oncol*. 2019;12(1):55. doi:10.1186/s13045-019-0770-1
12. Xia Y, Rao L, Yao H, et al. Engineering macrophages for cancer immunotherapy and drug delivery. *Adv Mater*. 2020;32(40):1. doi:10.1002/adma.202002054
13. Lei L, Cai SS, Zhang Y, et al. Structure inversion-bridged sequential amino acid metabolism disturbance potentiates photodynamic-evoked immunotherapy. *Adv Funct Mater*. 2022;32(21):57. doi:10.1002/adfm.202103394
14. Du J, Lane LA, Nie S. Stimuli-responsive nanoparticles for targeting the tumor microenvironment. *J Control Release*. 2015;219:205–214. doi:10.1016/j.jconrel.2015.08.050
15. Uthaman S, Huh KM, Park I-K. Tumor microenvironment-responsive nanoparticles for cancer theragnostic applications. *Biomater Res*. 2018;22 (1):22. doi:10.1186/s40824-018-0132-z
16. Jia QJ, Li ZZ, Guo CP, et al. PEGMA-modified bimetallic NiCo Prussian blue analogue doped with Tb (III) ions: efficiently pH-responsive and controlled release system for anticancer drug. *Chem Eng J*. 2020;2020:389.
17. Eshaghi MM, Pourmadadi M, Rahdar A, et al. Novel carboxymethyl cellulose-based hydrogel with core-shell Fe3O4@SiO2 nanoparticles for quercetin delivery. *Materials*. 2022;2022:15.
18. Di J, Gao X, Du Y, et al. Size, shape, charge and "stealthy" surface: carrier properties affect the drug circulation time in vivo. *Asian J Pharm Sci*. 2021;16(4):444–458. doi:10.1016/j.ajps.2020.07.005
19. Valencia-Lazcano AA, Hassan D, Pourmadadi M, et al. 5-Fluorouracil nano-delivery systems as a cutting-edge for cancer therapy. *Eur J Med Chem*. 2023;2023:246.
20. Caro C, Pourmadadi M, Eshaghi MM, et al. Nanomaterials loaded with Quercetin as an advanced tool for cancer treatment. *J Drug Deliv Sci Technol*. 2022;2022:78.
21. Han -S-S, Li Z-Y, Zhu J-Y, et al. Dual-pH sensitive charge-reversal polypeptide micelles for tumor-triggered targeting uptake and nuclear drug delivery. *Small*. 2015;11(21):2543–2554. doi:10.1002/smll.201402865
22. Zhou ZX, Liu XR, Zhu DC, et al. Nonviral cancer gene therapy: delivery cascade and vector nanoproperty integration. *Adv Drug Deliv Rev*. 2017;115:115–154. doi:10.1016/j.addr.2017.07.021
23. Wang J-Q, Yang Y, Cai C-Y, et al. Multidrug resistance proteins (MRPs): structure, function and the overcoming of cancer multidrug resistance. *Drug Resist Updat*. 2021;2021:54.
24. Fletcher JI, Haber M, Henderson MJ, et al. ABC transporters in cancer: more than just drug efflux pumps. *Nat Rev Cancer*. 2010;10(2):147–156. doi:10.1038/nrc2789

25. Li W, Zhang H, Assaraf YG, et al. Overcoming ABC transporter-mediated multidrug resistance: molecular mechanisms and novel therapeutic drug strategies. *Drug Resist Updat*. 2016;27:14–29. doi:10.1016/j.drup.2016.05.001
26. Wu JH, Batist G. Glutathione and glutathione analogues; Therapeutic potentials. *Gen Sub*. 2013;1830(5):3350–3353. doi:10.1016/j.bbagen.2012.11.016
27. Allocati N, Masulli M, Di Ilio C, et al. Glutathione transferases: substrates, inhibitors and pro-drugs in cancer and neurodegenerative diseases. *Oncogenesis*. 2018;2018:7.
28. Lin S-R, Chang C-H, Hsu C-F, et al. Natural compounds as potential adjuvants to cancer therapy: preclinical evidence. *Br J Pharmacol*. 2020;177(6):1409–1423. doi:10.1111/bph.14816
29. Pourmadadi M, Abbasi P, Eshaghi MM, et al. Curcumin delivery and co-delivery based on nanomaterials as an effective approach for cancer therapy. *J Drug Deliv Sci Technol*. 2022;2022:78.
30. Ahmad I, Khan MFA, Rahdar A, et al. Design and evaluation of pH sensitive PEG-protamine nanocomplex of doxorubicin for treatment of breast cancer. *Polymers*. 2022;2022:14.
31. Ashrafizadeh M, Hushmandi K, Mirzaei S, et al. Chitosan-based nanoscale systems for doxorubicin delivery: exploring biomedical application in cancer therapy. *Bioeng Transl Med*. 2022;2022:38.
32. Dosio F, Arpicco S, Stella B, et al. Hyaluronic acid for anticancer drug and nucleic acid delivery. *Adv Drug Deliv Rev*. 2016;97:204–236.
33. Bai Y, Liu C-P, Chen D, et al. beta-Cyclodextrin-modified hyaluronic acid-based supramolecular self-assemblies for pH- and esterase-dual-responsive drug delivery. *Carbohydr Polym*. 2020;2020:246.
34. Chen X, Liu Z, Parker SG, et al. Light-induced hydrogel based on tumor-targeting mesoporous silica nanoparticles as a theranostic platform for sustained cancer treatment. *ACS Appl Mater Interfaces*. 2016;8:15857–15863.
35. Fu H-G, Chen Y, Yu Q, et al. Polysaccharide-based nanoparticles for two-step responsive release of antitumor drug. *ACS Med Chem Lett*. 2020;11:1191–1195.
36. Gong G, Cao Y, Qian H, et al. Assessment of the antitumor activity of a cyclopalladated ferrocene compound assisted by a dual-targeting drug delivery system. *Chem Comm*. 2018;2018:54.
37. He J, Zhang W, Zhou X, et al. Reactive oxygen species (ROS)-responsive size-reducible nanoassemblies for deeper atherosclerotic plaque penetration and enhanced macrophage-targeted drug delivery. *Bioact Mater*. 2023;19:115–126.
38. Hadji H, Bouchemal K. Effect of micro- and nanoparticle shape on biological processes. *J Control Release*. 2022;342:93–110.
39. Haseli S, Pourmadadi M, Samadi A, et al. A novel pH-responsive nanoniosomal emulsion for sustained release of curcumin from a chitosan-based nanocarrier: emphasis on the concurrent improvement of loading, sustained release, and apoptosis induction. *Biotechnol Prog*. 2022;2022:38.